PNAS RESEARCH ARTICLE | APPLIED PHYSICAL SCIENCES

Nonequilibrium sensing of volatile compounds using active and passive analyte delivery

Soeren Brandt[a,b,1], Ida Pavlichenko[a,b,1], Anna V. Shneidman[a,1], Haritosh Patel[a,1], Austin Tripp[b], Timothy S. B. Wong[b], Sean Lazaro[b], Ethan Thompson[b], Aubrey Maltz[b], Thomas Storwick[b], Holden Beggs[b], Katalin Szendrei-Temesi[c,d], Bettina V. Lotsch[c,d], C. Nadir Kaplan[e,f], Claas W. Visser[g], Michael P. Brenner[a], Venkatesh N. Murthy[h,i], and Joanna Aizenberg[a,b,j,2]

Contributed by Joanna Aizenberg; received March 9, 2023; accepted June 22, 2023; reviewed by Teri W. Odom, Timothy M. Swager, and Alexander Tropsha

Although sensor technologies have allowed us to outperform the human senses of sight, hearing, and touch, the development of artificial noses is significantly behind their biological counterparts. This largely stems from the sophistication of natural olfaction, which relies on both fluid dynamics within the nasal anatomy and the response patterns of hundreds to thousands of unique molecular-scale receptors. We designed a sensing approach to identify volatiles inspired by the fluid dynamics of the nose, allowing us to extract information from a single sensor (here, the reflectance spectra from a mesoporous one-dimensional photonic crystal) rather than relying on a large sensor array. By accentuating differences in the nonequilibrium mass-transport dynamics of vapors and training a machine learning algorithm on the sensor output, we clearly identified polar and nonpolar volatile compounds, determined the mixing ratios of binary mixtures, and accurately predicted the boiling point, flash point, vapor pressure, and viscosity of a number of volatile liquids, including several that had not been used for training the model. We further implemented a bioinspired active sniffing approach, in which the analyte delivery was performed in well-controlled 'inhale-exhale' sequences, enabling an additional modality of differentiation and reducing the duration of data collection and analysis to seconds. Our results outline a strategy to build accurate and rapid artificial noses for volatile compounds that can provide useful information such as the composition and physical properties of chemicals, and can be applied in a variety of fields, including disease diagnosis, hazardous waste management, and healthy building monitoring.

sensors | machine learning | artificial noses | photonic crystals

Significance

Volatile compounds are used as markers of disease and food spoilage, indicators of the quality of indoor and outdoor air, and beacons for hazardous waste management. However, standard methods to determine and quantify the composition of gaseous samples rely on bulky and expensive equipment, while state-of-the-art portable sensors are still unable to accurately analyze a diversity of analytes and their mixtures. Here, we accentuate the differences between vapors by passively or actively controlling their delivery to a single mesoporous photonic sensor. The combination of gas dynamics, temporal signal collection, and machine learning allows us to classify volatile compounds, determine the composition of mixtures, and predict the properties of unknown volatiles.

The ability to sense a wide variety of volatile compounds and mixtures is essential to a broad range of industries, including agriculture (1); air, water, and food quality monitoring (2, 3); healthcare (4, 5); and hazardous material management (6, 7). Recent high-profile accidents involving toxic chemicals transport (e.g., hazardous spill in East Palestine, Ohio in 2023) motivate the need for increased safety and monitoring measures, in particular the development of small and inexpensive sensors that can rapidly and accurately identify analyte compositions and determine their physical and chemical properties on site. Although portable sensors are employed in practice, they tend to either be accurate for a specific subset of analytes (e.g., personal toxic gas safety monitors) or respond nondiscriminately to a range of analytes (e.g., chemiresistive sensors). Most of these are also unable to discern complex mixtures of components. This can be done with portable spectrometers; however, they have not yet reached the necessary maturity for operation by nonexperts due to the complexity of setting the sample-dependent measurement parameters (8).

Given these limitations, dogs are still employed in many practical scenarios such as following tracks, detection of bomb threats, and reclamation of contraband, highlighting the impressive capabilities of the natural olfactory system. Nature has indeed produced a versatile chemical sensor: The human nose can distinguish numerous odors at concentrations as low as 0.2 parts per billion (9). A variety of approaches have thus been proposed to create nose-inspired chemical sensors. The earliest designs mimicked biology's combinatorial approach in which odorants bind with differing strengths to more than one of the millions of odorant receptors (ORs), leading to odorant-specific patterns of OR excitation that the brain then interprets (10). Artificial implementations of this approach typically entail sensor arrays in which each sensor produces a distinct output for each odorant (11–13), or multivariable sensors (14), where one sensing element produces multiple independent outputs in response to each odorant. Each category has its own set of benefits and limitations, as depicted in Fig. 1*A*. Single sensors are the simplest to fabricate and relatively cheap, but they are usually unable to accurately discriminate different volatiles

Author contributions: S.B., I.P., and J.A. designed research; S.B., I.P., A.T., T.S.B.W., S.L., E.T., A.M., T.S., H.B., and K.S.-T. performed research; S.B., I.P., A.V.S., H.P., A.T., T.S.B.W., S.L., E.T., A.M., T.S., H.B., B.V.L., C.N.K., C.W.V., M.P.B., and V.N.M. analyzed data; and S.B., I.P., A.V.S., H.P., and J.A. wrote the paper.

Reviewers: T.W.O., Northwestern University; T.M.S., Massachusetts Institute of Technology; and A.T., University of North Carolina, Chapel Hill.

Competing interest statement: S.B., I.P., A.T., T.S.B.W., and J.A. are listed as inventors on the patent application US20210231558A1 and S.B., H.P., V.N.M., and J.A. on PCT/US2021/040126 related to the work described herein. All other co-authors have no competing interests to declare.

Copyright © 2023 the Author(s). Published by PNAS. This article is distributed under Creative Commons Attribution-NonCommercial-NoDerivatives License 4.0 (CC BY-NC-ND).

[1]S.B., I.P., A.V.S., and H.P. contributed equally to this work.

[2]To whom correspondence may be addressed. Email: jaiz@seas.harvard.edu.

This article contains supporting information online at https://www.pnas.org/lookup/suppl/doi:10.1073/pnas.2303928120/-/DCSupplemental.

Published July 26, 2023.

Downloaded from https://www.pnas.org by UNIVERSITEIT TWENTE CENTRALE BIBLIOTHEEK on January 9, 2024 from IP address 130.89.47.46.

due to the limited amount of information obtained from the sensor. The sensor array architecture works well in biology due to the molecular size of the receptors and their ability to regenerate, but artificial sensors tend to employ a small number of components that over time drift at different rates, thus requiring frequent sensor-specific recalibrations (15). Some recent approaches integrate molecular sensors directly, taking advantage of their small size to produce arrays with a small footprint (16–18), or —at a slightly larger length scale— employ arrays of advanced nanofabricated devices (19). In contrast, it is possible to account for and therefore reduce the effects of drift in multivariable sensors (20) though they can be difficult to fabricate (21). On their own, all of these types of sensors struggle to quantitatively characterize even simple mixtures of volatiles or require a complex and expensive fabrication procedure (21).

Hitherto, various techniques for unsupervised and supervised machine learning (ML) have been successfully applied to identify analytes from their intrinsic chemical spectra (e.g., NMR, Fourier-transform infrared spectroscopy, ultraviolet–visible spectroscopy, and Raman spectroscopy) (22–24).To further boost the performance of even simple single sensors, such as those depicted in Fig. 1, using ML, it is critical to provide the model with more nuanced input data. For example, in the biological olfactory system, information is provided to the brain not only from the equilibrium but also the transient response of the nose, namely, due to the unique mass transport dynamics exhibited by different odorants (25, 26). As described in Craven *et al.*, mass transport of odorants to and within the nose comprises a combination of 1) intranasal fluid dynamics within nasal cavities, convoluted nasal passageways, and a mucus layer, each of which embodies a passive transport modality, and 2) external aerodynamics in the form of active sniffing. In this spirit, artificial sensors have begun to use time-dependent dynamics of vapors interacting with the sensor to differentiate volatile compounds, for example, based on their rate of condensation or adsorption onto the sensing elements (27, 28). Porous photonic sensors with colorimetric readout or spectral shifts resulting from vapor adsorption can report on the dynamics characteristic to specific analytes (29–31). The time-dependent odor signatures are a result of the inherent physicochemical properties of odorants and their interaction with the porous material. Thus, by accentuating the differences in those properties, it is possible to improve the ability of the sensor to discriminate the odorants. In addition to extracting time-dependent signals from passive transport processes, mimicking biology's active control of odor transport in the form of sniffing has been used to reduce response time by guiding vapors towards the sensor and measuring the response to the onset, saturation, and periodic odor exposure (32–35). This unlocks the possibility to apply different *sniffing sequences* to actively modulate the dynamics of analyte delivery to the sensor, as well as to effectively gate its adsorption and desorption. Such an approach presents the opportunity to augment the discrimination between different odorants, as has recently been shown for the TruffleBot e-nose based on metal-oxide-semiconductor sensors to distinguish various alcohols (36).

In this work, we demonstrate discrimination of odors, determination of ratios of binary mixtures, and prediction of physical properties of analytes using time-dependent signals from a single mesoporous, one-dimensional photonic crystal (PhC) consisting of alternating layers of spun-coated silica and titania nanoparticles. We implement two different nonequilibrium approaches of analyte delivery: i) a passive approach, where the system is built to accentuate the differences in the mass transport of vapors emanating from a liquid drop in analogy to intranasal fluid causing concentration gradients in the nose, and ii) an active approach, where, inspired by sniffing, vapors are delivered to the sensor in short bursts (Fig. 1*B*, Step 1). As vapors enter the PhC pores, the reflection spectrum progressively redshifts due to an increase in effective refractive index of the layers (37–39). Time-dependent

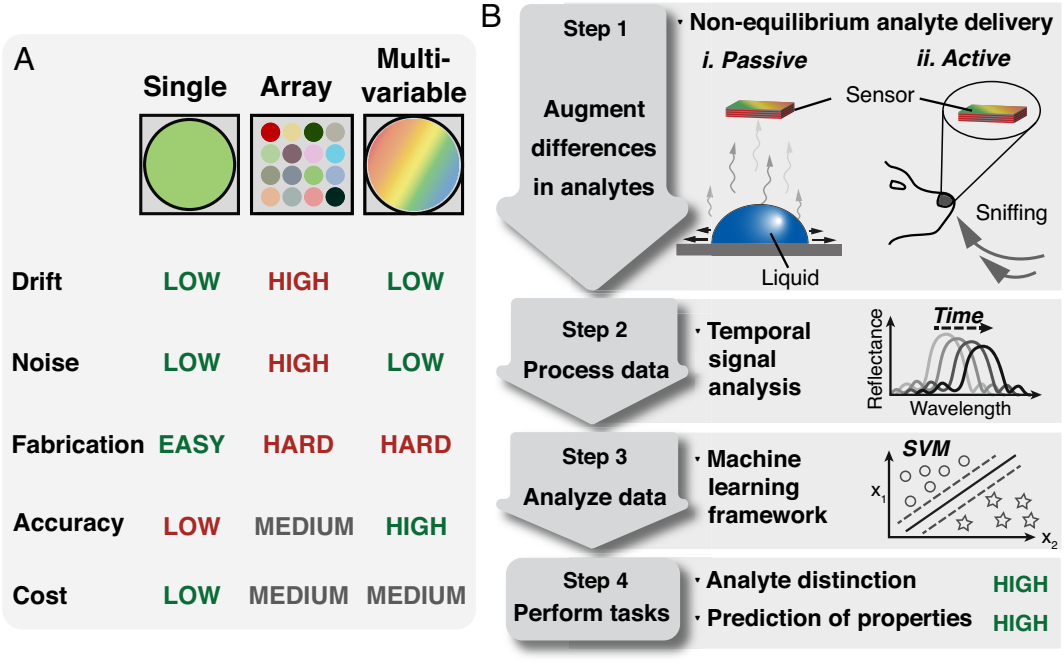

Fig. 1. Overview of sensor systems for volatile component detection. (*A*) Comparison of the typical performance of single sensors, combinatorial arrays, and multivariable sensors. (*B*) Our approach encompasses four steps: (Step 1) introduction of an analyte delivery modality that operates either i) passively or ii) actively, (Step 2) use of temporal signal processing, and (Step 3) implementation of machine learning analysis. Combining these three aspects greatly enhances the discriminatory power of any sensor system and allows for (Step 4) the differentiation of single component and multicomponent mixtures, and the prediction of their physical properties.

Downloaded from https://www.pnas.org by UNIVERSITEIT TWENTE CENTRALE BIBLIOTHEEK on January 9, 2024 from IP address 130.89.47.46.

processing of this signal using Fourier-transform feature (Fig. 1*B*, Step 2) and support vector machines (Fig. 1*B*, Step 3) allows us to successfully classify and quantify the composition of unary and binary mixtures with over 88% accuracy and R^2 of up to 0.95, respectively (Fig. 1*B*, Step 4).

By using ML, we also show the capability of predicting physical properties such as the boiling point, flash point, viscosity, and vapor pressure of organic compounds with low error in- and out-of-distribution. We demonstrate that modulating vapor injection in deliberate sniffing patterns accelerates odor detection and enables the utilization of desorption dynamics that can further improve delineation between similar odors. These capabilities will potentially further the detection of volatile compounds in challenging areas including the identification of unknown hazardous waste, contaminated liquids, oil samples, and disease diagnosis using a real-time sensor system.

Results

Passive Vapor Delivery. The passive analyte delivery system is shown schematically in Fig. 2*A* and presented in more detail in *SI Appendix*, Fig. S1 and Note S1. It consisted of a glass chamber with a blunt-tipped needle attached to its top to deposit the analyte liquid. Our optical sensor, here a mesoporous one-dimensional PhC (Bragg stack), was attached to the inner surface of the top of the chamber. The PhC was prepared by spin-coating 11 alternating layers of silica and titania nanoparticles (39). It displays bright coloration due to the large refractive index (n) contrast between the materials comprising the different layers (silica nanoparticles $n \sim 1.5$ and titania nanoparticles $n \sim 1.9$, Fig. 2*B*, see *Materials and Methods* for the PhC fabrication). The gaps between the PhC nanoparticles form small pores of ~10 nm, promoting condensation of the analyte vapors (40, 41). The thickness of the adsorbed layer depends on a variety of factors, notably the relationship between the disjoining pressure, which describes the attractive forces between the liquid and the surface, and the partial pressure of the vapor (42).

Early work in photonic VOC sensing predominantly involved static analysis in which the presence of a gas was determined by analyzing the reflection spectrum before and after adsorption (i.e., snapshots of the spectra). However, differences in reflection spectra between different gases after adsorption tend to be too small to discern, as their refractive indices differ only slightly (*SI Appendix*, Table S1), and vapor concentrations in the PhC are low. In contrast, the dynamics of adsorption can be quite distinct due to differences in equilibrium vapor pressure, thus driving capillary condensation at different pressures and therefore at different times in the diffusion process. We intentionally magnified these differences by spatially separating the liquid injection site from the PhC, thus delaying the time between stabilization of the vapor concentration in the chamber and adsorption reaching steady state, defined here as the time beyond which the reflection spectrum of the crystal no longer changes appreciably. Schlieren imaging was used to observe the vapor transport within the chamber leveraging the ability of this technique to detect slight differences in refractive index (as shown for pentane in Fig. 2*C*, red line denotes the calculated diffusion front; details of the imaging and image analysis are provided in *SI Appendix*, Note S1). We found that the vapor front transport corresponds to a dominantly diffusion-based transport (*SI Appendix*, Fig. S2). In each experiment, we dispensed

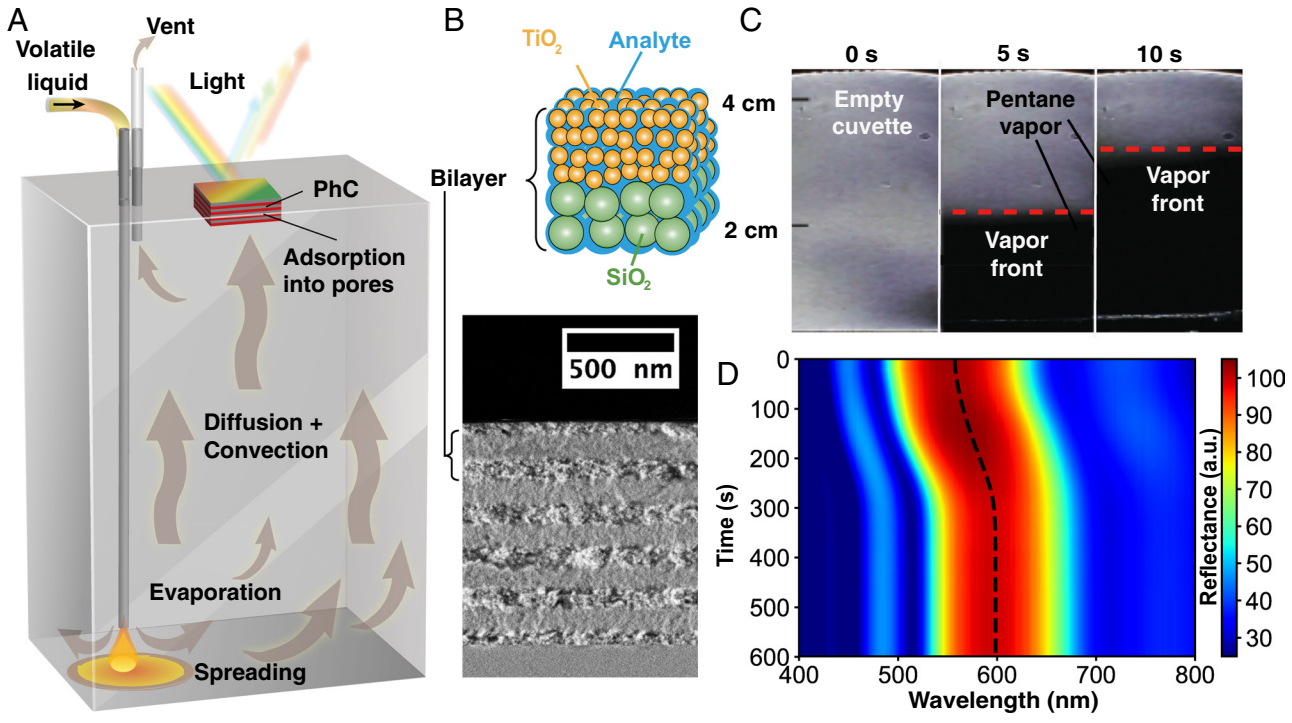

Fig. 2. Sensor design and temporal analysis for volatile liquids with passive analyte delivery. (*A*) Schematic of the sensor system consisting of a syringe to dispense the volatile liquid, a glass chamber, and photonic crystal (PhC); a white light source and spectrophotometer (not depicted) collect the time-dependent reflection spectrum from the PhC. Arrows indicate the diffusive-convective vapor transport from the bottom of the chamber to the optical sensor at the top. (*B*) Schematic illustration (*B*, *Top*) and scanning electron microscopy (SEM) image (*B*, *Bottom*) of a cross-section of the PhC, showing its alternating silica and titania layers. Here, the PhC consists of 5.5 bilayers. (*C*) Schlieren microscopy images show the initial time-resolved vapor transport of pentane (appears as a dark area) in the chamber. The red lines indicate the diffusion lengths at 5 and 10 s, corresponding to the vapor front in a diffusion model. (*D*) River plot of the PhC reflectance spectrum recorded over a 10-min experiment with pentane as the volatile liquid. The dotted line superimposed on the river plot illustrates the evolution of the redshift over time and was obtained from the feature (Ψ) used to train the ML algorithm.

Downloaded from https://www.pnas.org by UNIVERSITEIT TWENTE CENTRALE BIBLIOTHEEK on January 9, 2024 from IP address 130.89.47.46.

1 mL of the liquid analyte at a constant rate of 6 mL min^{-1} for 10 s, ensuring that the liquid formed a thin layer rather than a droplet, preventing an evaporation gradient that would result from curvature at the liquid–air interface. Liquid dispensed by the syringe impinges on the bottom of the chamber where its spreading rate depends on its surface tension and the surface energy of the chamber bottom. Following spreading, the liquid partly evaporates, resulting in vapor which diffuses and spreads through the chamber, gradually infiltrating the PhC, and therefore producing a redshift of the reflection spectrum over time as the quantity of vapor condensed within the PhC pores continues to increase (Fig. 2*D*).

Temporal Data Analysis. The time-dependent reflection spectrum of the PhC was collected over 10 min for each analyte. We found that tracking the wavelength corresponding to the highest intensity peak, $\lambda_{peak}(t)$, provides meaningful differences between the compounds. As the peak is rather broad, λ_{peak} was determined at each time point by applying a discrete Fourier Transform (FT) in reciprocal wavelength space to the intensity [I(λ, t)] and using Ψ(t), defined as the sine of the phase of the lowest nonzero frequency component of the FT scaled to the wavelength (*SI Appendix*, Figs. S3 and S4 and Note S2 provide the definition of Ψ and additional details of the data processing pipeline). Previously a wavelet transform, which transforms features localized in both frequency and time, has been used to analyze the evolving reflection spectrum from a mesoporous silicon PhC in response to imposed temperature changes (36, 43). Although the wavelet transform is well-suited to detect changes in the spectrum over time, we found the transformed data become challenging to interpret when the experimental variance is high, e.g., in the case of nonuniformities of a PhC created using standard laboratory-scale methods such as spin-coating, where the layer thickness can vary across the sensor.

Ψ(t) is plotted as a dashed line in Fig. 2*D*, and it indeed follows the measured $\lambda_{peak}(t)$. For analysis of passive sensing, the discrete time derivative of Ψ – hereafter, denoted as $\Delta\Psi/\Delta$t – was calculated to remove information regarding the exact location of the initial peak, i.e., $\lambda_{peak}(t = 0$ s). It is interesting to note that $\Delta\Psi/\Delta$t already qualitatively distinguishes polar vs. nonpolar volatiles as nonpolar analytes exhibited a smooth peak in $\Delta\Psi/\Delta$t between 75 to 300 s (the small peak that can be seen occasionally just after ~10 s is likely an artifact of the analyte injection before 15 s). $\Delta\Psi/\Delta$t for the polar compounds (with the exception of water) exhibited a sharper peak earlier on, reaching a maximum value between 30 to 75 s, followed by a second broader maximum (Fig. 3*A*). We attribute the two peaks to the two-step adsorption process for polar compounds into the mesoporous PhC, in which their favorable vapor–surface interactions with the hydrophilic surfaces of silica and titania of the crystal lead to 1) the formation of a monolayer before 2) condensing into a film, consistent with previous findings based on measurements of adsorption isotherms (44–46), as well as our own measurements for the nonpolar compounds (*SI Appendix*, Fig. S5 and Note S3). The latter, due to relatively weak adsorbent–adsorbate interactions, feature a single-step adsorption isotherm shape, likely due to a competition between monolayer and multilayer formation or molecular cluster formation en route to multilayers. Water, in contrast to other polar compounds, produced a unique profile consisting of a single peak with a left shoulder. There is evidence that water is adsorbed simultaneously within titania and silica pores at lower partial pressures (below 0.4), as opposed to preferential and gradual adsorption of polar hydrocarbons first onto the titania smaller pore walls, with subsequent adsorption to both layers at higher pressures (above 0.7) (38). Note that if the change of reflectance is compared only between the initial and final timepoints, as in static analysis, the curves are practically indistinguishable (*SI Appendix*, Note S4), and thus would not allow the discrimination between the liquids, confirming a significant benefit of using time-resolved analysis for vapor sensors.

ML for Classification of Analytes. We trained a Support Vector Machine (SVM) for classification and regression tasks using the normalized input vectors $(\Delta\Psi/\Delta t)_{norm}$ for different vapors. An SVM is a ML algorithm that determines a hyperplane that maximally separates unique classes, in this case volatile compounds. Each of the vectors contains 600 elements (one per second in the 10-min interval over which experiments were recorded) and was normalized using the L2-norm. The dataset

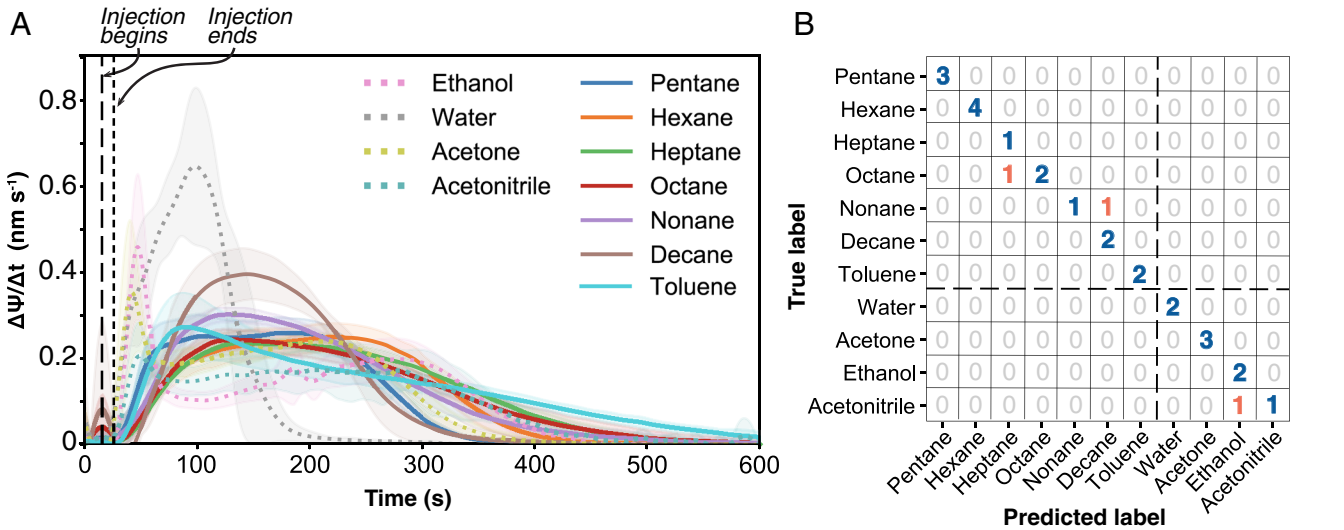

Fig. 3. Temporal analysis and training of a Support Vector Machine (SVM) to distinguish volatile compounds. (*A*) $\Delta\Psi/\Delta$t is calculated from the temporal evolution of the reflectance spectrum of the PhC upon exposure to one of 11 volatile compounds, with the liquid injection occurring at ~15 s, and ending at ~25 s, as indicated by the two dashed vertical lines. The solid and dotted curves indicate nonpolar and polar solvents, respectively. For each, the line represents the mean of the dataset and the shaded region represents the standard deviation (SD). (*B*) Confusion matrix for temporal analysis demonstrates 23 correct predictions out of 26 test samples.

Downloaded from https://www.pnas.org by UNIVERSITEIT TWENTE CENTRALE BIBLIOTHEEK on January 9, 2024 from IP address 130.89.47.46.

consisted of ten pure volatile organic compounds (VOCs) and water: seven nonpolar compounds (linear alkanes from pentane to decane and toluene), as well as four polar compounds (water, ethanol, acetone, and acetonitrile), $\Delta\Psi/\Delta t$ profiles depicted in Fig. 3*A*. We performed a total of 76 experiments with the number of experiments per compound varying between 3 and 10 and split the dataset into 50 training and 26 testing examples (*Materials and Methods* and *SI Appendix*, Table S2). The SVM correctly identified 23 out of 26 test examples (88% prediction accuracy, Fig. 3*B*, see cross-validation analysis in *SI Appendix*, Fig. S6). The model confidently distinguished polar from nonpolar compounds, highlighting the observation that the shape of the $\Delta\Psi/\Delta t$ depends on the physicochemical properties of the compound. As a control procedure, when using the same train-test-split approach and using only the change in reflectance between the initial point and the steady state, we observed that the accuracy dropped by more than half (38% prediction accuracy, *SI Appendix*, Fig. S7), reiterating the usefulness of temporal data collection and analysis.

Support Vector Regression (SVR) to Quantify Binary Mixtures. To go beyond classification of pure compounds, we tested our ability to predict the composition of binary mixtures using the passive sensor delivery together with SVM. We chose to focus on the alkanes as they readily mix and the behaviors of their mixtures depend predominantly on differences in molecular lengths. For example, pentane and hexane form nearly ideal mixtures, as determined by the nearly linear change in the vapor pressure as a function of the mixing ratio (47), whereas pentane–octane mixtures deviate more from ideality, and there is a significantly higher relative proportion of pentane in the vapors of the latter than the former (48).

The training data for the SVR consisted of $(\Delta\Psi/\Delta t)_{norm}$ for each of the binary mixtures of n-alkanes. $(\Delta\Psi/\Delta t)_{norm}$ for the pentane-hexane mixtures showed a monotonic decrease in the time to reach steady state with increasing pentane concentration (Fig. 4*A*). In contrast, the change in time to steady state for pentane–octane mixtures was nonmonotonic (Fig. 4*B*), likely related to the differences in vapor condensation in the pores of the photonic crystal. Specifically, published isotherms (40) and our measurements (*SI Appendix*, Fig. S5*C*) for alkanes indicate that heavier compounds condense in the pores of the photonic crystal at lower relative pressures than lighter ones, reported for octane vs. hexane. We hypothesize that as the heavier alkane, octane, condenses at lower relative pressures, it could induce faster kinetics of the adsorption-driven spectrum shift than the mixture with the lighter alkane, hexane. The presence of octane would thus lead to the observed increased diversity of shapes of $(\Delta\Psi/\Delta t)_{norm}$, which in turn may contribute to a higher R^2 of the SVRs: R^2 of 0.76 for pentane–hexane (Fig. 4*C*) vs. 0.95 (Fig. 4*D*) for pentane–octane. Overall, we observed a high sensitivity to slight changes in composition of binary mixtures on the order of a few parts-per-million (*SI Appendix*, Fig. S8 and Note S5). This sensitivity underlines the richness of information that can be obtained from temporal analysis of the porous PhC sensor adsorption dynamics.

Prediction of Physical Properties of Volatiles. In addition to identifying the composition of binary mixtures, this approach also enables the assessment of physicochemical properties of volatiles. We demonstrated this by predicting the boiling point, flash point, viscosity, and vapor pressure for the pure alkanes tested above (*SI Appendix*, Note S6) through training four instances of SVRs (one for each physical property) using a radial basis function kernel on the $(\Delta\Psi/\Delta t)_{norm}$ of the alkane data (pentane, hexane, heptane, octane, nonane, and decane; 38 experiments total). The data were labeled with the true value of the relevant physical property (*SI Appendix*, Table S3). The training set contained 25 out of the 38 measurements with 2 to 6 examples for each alkane. The model was then tested on separate experimental measurements of the same compounds using a random split. We were able to

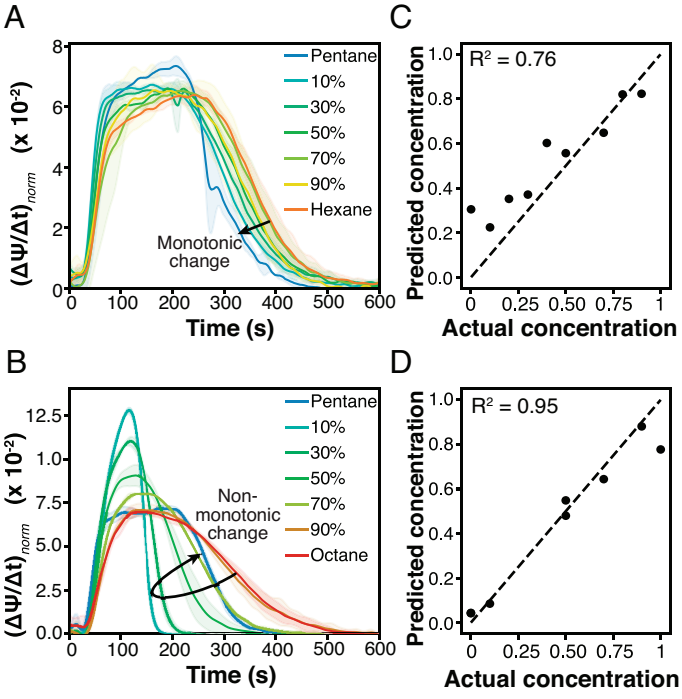

Fig. 4. Predictability of chemical composition from temporal data $(\Delta\Psi/\Delta t)_{norm}$ for (*A*) pentane–hexane mixtures showing a monotonic decrease in the duration of the adsorption process with increasing pentane content (vol./vol.) and for (*B*) pentane–octane mixtures showing a pronounced nonmonotonic behavior. (*C, D*) SVR prediction performance for (*C*) pentane–hexane and (*D*) pentane–octane mixtures based on training on $(\Delta\Psi/\Delta t)_{norm}$ in *A* and *B*, respectively. The number of points in *C* and *D* differ due to the different sizes of the datasets for pentane–hexane vs. pentane–octane mixtures.

Downloaded from https://www.pnas.org by UNIVERSITEIT TWENTE CENTRALE BIBLIOTHEEK on January 9, 2024 from IP address 130.89.47.46.

predict the physical properties of the remaining 13 measurements with extremely high accuracy, yielding R^2 values of 0.94, 0.94, 0.81, and 0.92, for boiling point, flash point, viscosity, and vapor pressure, respectively (Fig. 5*A*). The four physical properties were chosen due to their relationship to the vapor dynamics, which are essentially encoded in $(\Delta\Psi/\Delta t)_{norm}$. The ability of the SVR to reliably predict flash point is consistent with Vidal et al in which it was shown that for pure liquids, the prediction of flash point can be related to the vapor–liquid equilibrium and mass transfer in the apparatus (49).

We further explored the possibility to characterize volatiles 'unknown' to the SVR, i.e., they were not part of the training set (Fig. 5*B*). Specifically, we predicted the physical properties of toluene, cyclohexane, dichloromethane, and the polar compounds based on training on the alkane feature vectors only. Toluene and cyclohexane were of particular interest as they have molecular weights (MWs) in the range of the alkanes used for training and all of their physical properties are contained within the range of values seen by the ML model in training. Their molecular structure is, however, sufficiently different from the linear alkanes, causing the intermolecular forces (IMFs), and therefore the vapor dynamics, to be different. For example, as a cyclic aromatic hydrocarbon, toluene's IMFs are strengthened by π-π interactions, resulting in slower evaporation and prolonged condensation in the PhC. Toluene is thus an excellent test candidate, being dissimilar enough from the alkanes to demonstrate that the prediction is not a simple interpolation from the training data. Meanwhile, the cyclic alkane, cyclohexane, experiences the same types of IMFs as the linear alkanes (London dispersion forces), yet is slightly less volatile than its linear counterpart, hexane, due to the differences in the geometries of the two molecules and therefore the strength of the IMFs. Using the trained SVR from Fig. 5*A*, we predicted the physical properties of toluene: boiling point to be 118.3 ± 8.1 °C (vs. published value of 110.6 °C); flash point to be 7.1 ± 5.3 °C (vs. 4.4 °C); viscosity to be 0.47 ± 0.02 mPa·s (vs. 0.56 mPa·s); and vapor pressure to be 11.2 ± 3.5 kPa (vs. 3.4 kPa). For cyclohexane we predicted: boiling point to be 80.8 ± 6.7 °C (vs. published value of 81.0 °C); flash point to be −17.0 ± 4.7 °C (vs. −20.0 °C); viscosity to be 0.38 ± 0.01 mPa·s (vs. 0.89 mPa·s); and vapor pressure to be 16.6 ± 1.7 kPa (vs.11.9 kPa).

The accuracy of the toluene and cyclohexane predictions is encouraging given that the SVR has only been trained on alkane data. In fact, the root-mean-squared errors for toluene and cyclohexane predictions were almost identical to those for n-alkanes, with the exception of vapor pressure for toluene and viscosity for cyclohexane. It is worth mentioning that since the IMFs —and therefore the vapor dynamics— of linear alkanes correlate with their MW (*SI Appendix*, Table S3), one could surmise that the prediction accuracies for cyclohexane and toluene would be expected since their MWs are between those of pentane and hexane, or those of hexane and heptane, respectively. However, our ML model was trained on the vapor dynamics and not on the the MW, chemical structure, or chemical formula. The discrepancy in predictions vs. true values for toluene's vapor pressure and cyclohexane's viscosity likely stem from

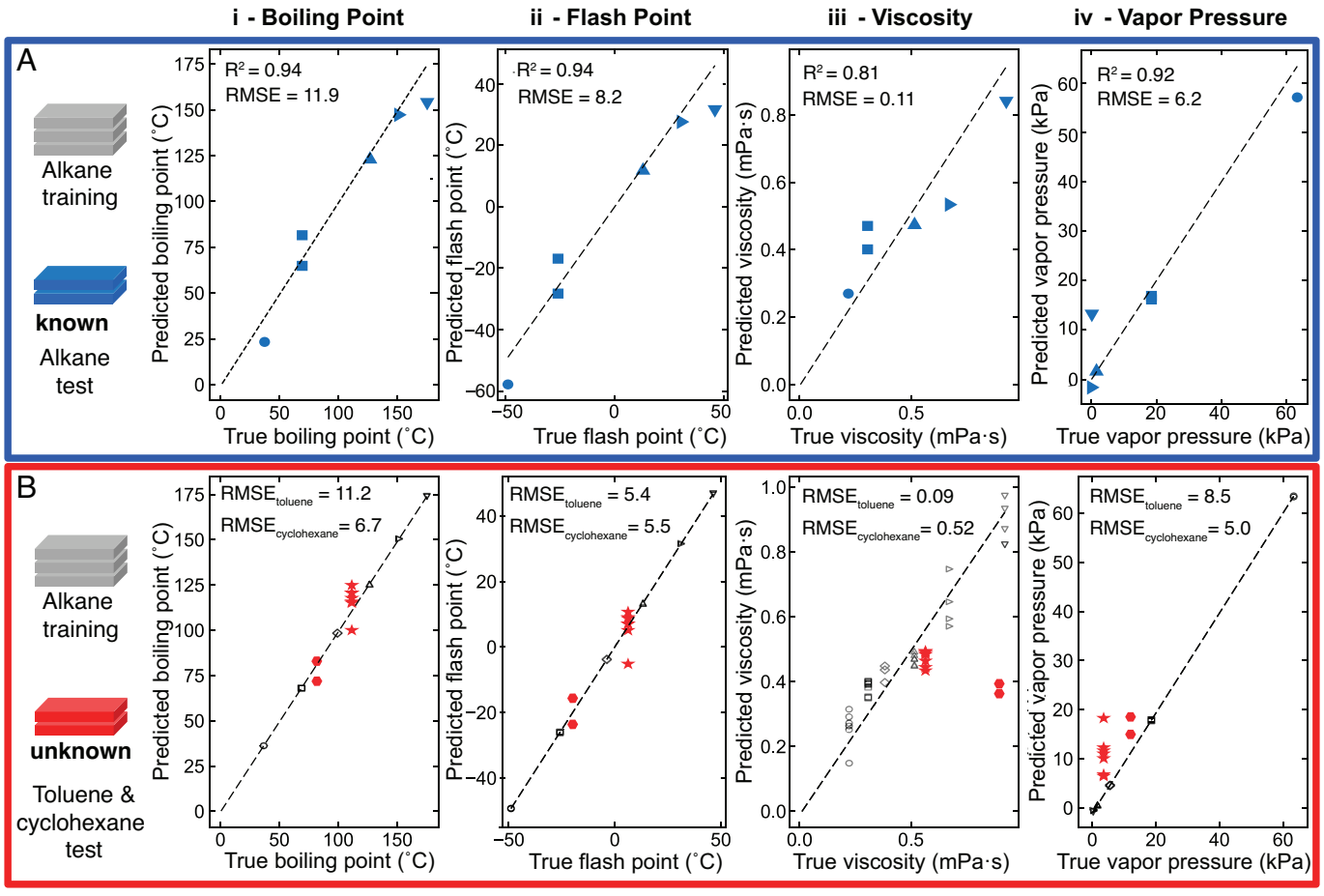

Fig. 5. Prediction of physical properties from temporal reflectance data. (*A, B*) Regression plots showing results of SVR training on n-alkanes to predict the properties of (*A*) a test set of alkanes (● pentane, ■ hexane, ♦ heptane, ▲ octane, ► nonane, and ▼ decane) and (*B*) volatiles 'unknown' to the SVR such as toluene (red stars) and cyclohexane (red hexagons), where empty symbols signify alkane training data.

Downloaded from https://www.pnas.org by UNIVERSITEIT TWENTE CENTRALE BIBLIOTHEEK on January 9, 2024 from IP address 130.89.47.46.

the natural limitation of the ML model trained only on the alkane dataset. We hypothesized that the trained SVR utilized the temporal information from the strongest shift between 50 and 250 s (*SI Appendix*, Fig. S9). In toluene's case, the broad range of vapor pressure in the training data (spanning two orders of magnitude) and the comparatively low vapor pressure of toluene make the real value difficult to predict. The consistently higher predicted vapor pressure for toluene may be due to the elongated shape of its $(\Delta\Psi/\Delta t)_{norm}$ relative to those of the alkanes (Fig. 3 and *SI Appendix*, Fig. S10). For cyclohexane, the problem stems from high similarity of its $(\Delta\Psi/\Delta t)_{norm}$ to the ones of hexane and heptane, especially in the region of highest feature weights of the SVR's kernel (*SI Appendix*, Fig. S11). Given the limited training, the ML was unable to predict cyclohexane's relatively high viscosity (0.89 mPa·s) that is much closer to decane's viscosity (0.92 mPa·s) than to that of its closest structural analog, hexane (0.30 mPa·s). Last, we also evaluated the ability of the SVR only trained with n-alkanes to predict the properties of polar compounds, and found that the out-of-distribution accuracy was —unsurprisingly— further reduced, due to the highly dissimilar, typically dual-modality, shape of $(\Delta\Psi/\Delta t)_{norm}$ for the polar analytes (*SI Appendix*, Fig. S12). The model's sensitivity to the unique shapes of $(\Delta\Psi/\Delta t)_{norm}$ (capturing information about the vapor dynamics) suggests that the SVRs identify correlations between the measured signal and the underlying molecular properties of the analyte, a combination of its size, geometry, polarity, and other aspects.

Active Control of the Vapor Dynamics for Faster Sensing Using Sniffing. The experiments described thus far had not incorporated sniffing behaviors used by animals to accelerate the delivery of vapors to the sensory receptors (50), which reputedly provides additional information to aid odor discrimination (51). We assembled a separate system to demonstrate artificial sniffing (*SI Appendix*, Fig. S13 and Note S7). The PhC was attached to the top of a chamber, and vapor was delivered via pressurized nitrogen carrier gas injection whose flow was controlled by solenoid valves, with the opening and closing of valves mimicking different sniffing patterns composed of inhalation of duration t_{in} (dry nitrogen was passed through a vial containing the analyte), short waiting periods for time t_w (inlet flow was stopped), and exhalation over time t_{ex} (dry nitrogen without analyte was passed continuously through the chamber containing the sensor, promoting analyte desorption). The schematic above the plot in Fig. 6*A* shows an example sniffing sequence consisting of five repetitions of "short sniffs" (t_{in} = 1 s, t_w = 0.5 s) followed by an exhale (t_{ex} = 5 s). We compared the results of this sniffing sequence for the different alkanes, from pentane to decane, as a proof of concept (Fig. 6*A*, plot). Because the outlet of the chamber was open over the duration of the experiment, the concentration of the vapor in the chamber slightly decreased during the waiting steps and never fully equilibrated, reminiscent of the phenomenon of "breath stacking" observed in the sniffing of dogs, in which they take in more air than they expel during each sniff (26). We also separately validated the ability of the PhC sensor to respond with a time scale of less than one second (*SI Appendix*, Fig. S14) to ensure that we can capture all significant spectral changes within the acquisition time.

In this active delivery approach, we chose to train the SVM using Ψ_{norm} rather than $(\Delta\Psi/\Delta t)_{norm}$ that had been used in the passive delivery scenario. Our motivation stems from the differences in the vapor dynamics, described in detail in *SI Appendix*, Fig. S15 and Note S8. Here, the vapor fills the chamber and begins adsorption within the PhC during inhales which decreases and ultimately transitions to desorption during wait steps and exhales, the signatures of which are imposed on the shape of Ψ_{norm} (Fig. 6*A*). Alkanes saturated the PhC in order of their chain length, with the shortest, most volatile alkanes saturating the PhC most quickly. Following saturation, Ψ_{norm} oscillated near its maximum value due to the slight loss of air from the chamber during the wait periods. The heavier alkanes also took significantly longer to desorb, as observed by their slower decay of Ψ during the exhale period (8 to 12 s) than for the shorter alkanes. In contrast to the case of passive experiments, which were conducted over 10 min, the alkanes were distinguishable with high confidence, with the exception of hexane, within the short experiment time of only 12.5 s (95% accuracy, Fig. 6*B*). Based on prior findings of Spencer et al regarding the effect of air flow on the sensitivity of chemical detection, we hypothesize that future experiments with higher frequency sniffing patterns (shorter sniffs, *i.e.* shorter t_{in} and t_w) could further improve differentiation between the more volatile VOCs (e.g., here: pentane, hexane, heptane) and their mixtures by spreading out the total change in Ψ_{norm} over smaller increments and prolonging the time to saturation (35). Less volatile compounds would be better detected when deeper sniffs (i.e., longer t_{in}) are implemented, in order to accumulate those compounds at the sensor to an appreciable concentration.

Thus, by adjusting the sniffing pattern, it is possible to tweak the protocol for the specific task, and potentially could be applied to sequentially pick out different components of a mixture. As a demonstration of this approach, we showed the unique sensor response to pentane and ethanol via different sniffing sequences (Fig. 6 *C* and *D*, respectively). For pentane, we saw a pronounced difference when switching between short and deep sniffing sequences (Fig. 6*C*). However, for ethanol, the same change in sniffing sequence did not alter the sensor response. By screening through a repertoire of possible sensing protocols (e.g., changing times of each step, whether the system is open or closed, the total duration of the measurement, etc.), we found that performing a single short sniff followed by a longer exhale (t_{ex}= 10 s) led to a clearly different signal (Fig. 6*D*). Last, utilizing five repetitions of short sniffs (t_{in} = 1 s, t_w = 0.5 s) followed by an exhale (t_{ex} = 5 s), we demonstrated the ability to determine the mixing ratio of pentane-octane mixtures with R^2 of 0.88; an exceptional regression given only a ~12 s detection period (*SI Appendix*, Fig. S16 and Note S9). Together, these results suggest a generalized approach that increases the differences in response between analytes as elaborated in the discussion.

Discussion

This work takes steps toward addressing a challenge in the design of artificial noses: obtaining feature-rich and interpretable information from the vapor of an analyte using only one sensing device. By recording the time-dependent response of a porous photonic sensor to the passive transport of vapors or their actively controlled delivery, we determined that the time-resolved feature Ψ, or its derivative $\Delta\Psi/\Delta t$, is sufficient to classify and make deterministic predictions of the components and properties of vapors. Using support vector machines, we were able to classify 10 volatile liquids and water with 88% accuracy and predict the mixing ratios of binary mixtures of pentane–hexane and pentane–octane (R^2 of 0.76 and 0.95, respectively), and even achieve parts-per-million resolution in binary mixtures of ethanol-water.

Although sensor arrays have been demonstrated with accuracies greater than 95% (52), *it is important to highlight that our results are all obtained from a single sensor*. In addition, although our classifier is currently limited to the detection of reference analytes previously seen by the SVM, the regression models allow predicting the boiling point, flash point, viscosity, and vapor pressure of

Downloaded from https://www.pnas.org by UNIVERSITEIT TWENTE CENTRALE BIBLIOTHEEK on January 9, 2024 from IP address 130.89.47.46.

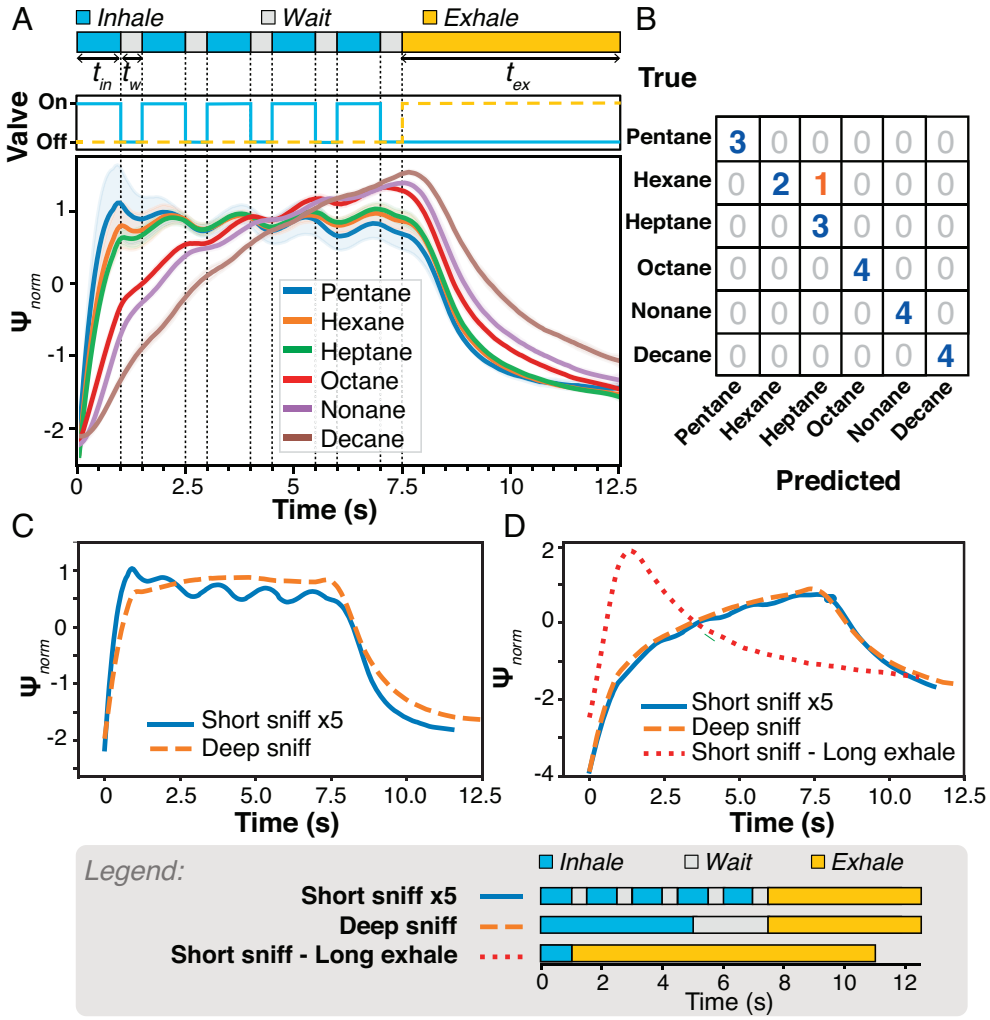

Fig. 6. Demonstration of sniffing protocols to accentuate alkane odor signatures. (*A*) Temporal analysis of active delivery using Ψ_{norm} for linear alkanes. Blue solid and yellow dashed lines represent the on/off status of the solenoid valves corresponding to the inhale and exhale periods. (*B*) Confusion matrix for temporal analysis demonstrates 20 correct predictions out of 21 test samples. (*C* and *D*) Demonstration of various sniffing sequences: "short sniff x5" (i.e., repeat the "sniff" {t_{in}= 1 s, t_w= 0.5 s} 5 times, concluding with t_{ex}= 5 s), "deep sniff" (t_{in}= 5 s, t_w= 2.5 s, t_{ex}= 5 s), and "short sniff-long exhale" (t_{in}= 1 s, t_{ex}= 10 s) for (*C*) pentane and (*D*) ethanol.

some "unknown" compounds, e.g., toluene and cyclohexane, that the model trained on alkanes had not seen before. This indicates learning of the volatiles' physicochemical nature rather than the model simply understanding a nonphysical feature description. This enables adapting the approach to applications where a full dataset of possible compounds cannot be cataloged, such as in hazardous waste management. As shown by the limitations of the approach to accurately predict the physical properties only of relatively similar compounds to those used in training, it will be important to include a sufficiently broad —but not necessarily exhaustive— set of compounds in the training set to cover a wide enough range of features for the target application. A potential example of practicality of our approach would be to test the important properties for safe handling of crude oil. Blended from different source wells before it is shipped, crude oil represents a highly variable mixture with respect to physical properties and hence the packing group (*SI Appendix*, Note S10) and relevant safety precautions (53). Quantification of the relationship between the evaporation of highly volatile pentane-hexane and less volatile pentane–octane liquid mixtures, as presented here using the temporal signal from a mesoporous PhC, represents a proxy scenario for a potential time-resolved sensor to categorize hazardous flammable liquids by their relevant properties (e.g., vapor pressure, boiling point, flash point) in a realistic environment.

There are many avenues for further improving the odor discrimination power of our sensor for various applications. Continuing in the spirit of this work, a particularly fruitful route is to consider even more details of the natural olfactory system. Biological olfaction employs numerous design features to promote odor discrimination. The orientation of nostrils, as well as nasal size and geometry, vary across animals and likely depend on how critical this sensory modality is to the organism's survival, as well as on the environment to which it is exposed (e.g., marine, underground, surface, and in-flight). The epithelium and mucus layers, which cover the nasal passageways, warm and humidify the incoming air (54, 55) and it is widely believed, based on the sorption hypothesis, that these layers produce a chromatographic effect such that the adsorption of different odorants varies within the nasal passageway (51).

Like in the biological nose, multiple mass transport processes are involved in the presented artificial sensor —here, spreading, evaporation, convection, diffusion, and adsorption— each of which can be modulated. We explored several parameters of our sensor architecture. By changing the nanoparticle size in each

Downloaded from https://www.pnas.org by UNIVERSITEIT TWENTE CENTRALE BIBLIOTHEEK on January 9, 2024 from IP address 130.89.47.46.

layer, and thereby changing the overall PhC porosity, the adsorption of vapors is affected, leading to a change in the evolution of Ψ and the signal strength over time (*SI Appendix*, Fig. S17 and Note S11) (41, 56). Both a higher sensitivity and resolution can be achieved by varying the number of layers in the PhC or their refractive index, as this would change the width and intensity of the main reflectance peak (44). Altering the interaction of the surface of the chamber bottom via either chemical or physical modifications will affect spreading of the liquid on the sensor bottom (*SI Appendix*, Fig. S18), which in turn will affect evaporation due to its dependence on the curvature of the dispensed drop and area over which the evaporation occurs. Furthermore, variation of the porosity, surface functionalization, material composition, or a combination of those across one or multiple PhC sensors may further enhance the chromatographic effect, i.e., the differences in rates of condensation of different vapors within the PhC's porous layers. The temporal sensor itself could also actively modulate the signal: for example, a PhC made from responsive materials would exhibit changes in the pore sizes and layer spacing upon imposed changes in humidity or temperature (57), resulting in dynamic changes in absorption; this is similar to the swelling of the epithelial lining of the nose, which is known to increase the flow resistance in one nostril compared to another and may be used to provide additional information to the brain (58). Another aspect that can be changed is the geometry of the chamber, similar to the role the size of nasal passageways and cavities in nature play in odor discrimination. For example, by increasing the chamber height, we provide a longer path length for mass transport of the vapors, which, in turn, affects the time-evolution of the reflection spectrum (*SI Appendix*, Fig. S19). As indicated in the results section, cosolvents can also be added to increase the sensitivity to compounds contained in mixtures; when water is used, this is akin to humidifying the air as it passes through the nose of an organism. Likewise, for alkanes, we observed that a small amount of octane could increase the sensitivity of the sensor to pentane. Each of these changes would be relevant to both the passive and active analyte delivery modalities.

In addition to modifying the sensor design, emphasis should also be put on ML and signal processing. While we did limit our discussion to SVMs due to the scope of the available training data, different architectures for neural networks and deep learning can be optimized for feature recognition and physical processes (59). Using a larger training dataset, neural networks and automatic feature extraction could prove superior (60). For example, one approach may include artificial noses that implement biologically inspired sniffing sequences and incorporate artificial intelligence to analyze sensing results and optimize sniffing sequences in real-time based on continuous feedback algorithms. This is similar to the way dogs modify their sniffing frequency based on the types of analytes they smell and the bits of information they piece together in sequential breaths (61).

Many industries that require a simple, portable, low-cost sensor could benefit from our approaches. Example applications include identifying hazards on site, monitoring air quality, ensuring healthy building spaces (62), and point-of-care breath analyzers for rapid diagnosis of diseases for which characteristic volatiles have been identified (63, 64). In fact, the need to acquire real-time information about the air we breathe, both indoors and outdoors, has been brought into the spotlight by recent events such as wildfires, the SARS-CoV-2 pandemic, large spills, and growing concerns as well as regulations regarding air pollution (65). It has thus become abundantly clear that sensing-based ventilation and cleaning will be the future to ensure healthier building spaces (62), targeting both acute events as well as persistent issues such as presence of mold and other pollutants. Using sniffing for sensing is an exciting direction, opening doors to employing sniffing-related behaviors seen in nature, such as adapting sniffing frequencies to detect specific odorant types, for sensing capabilities and applications.

Materials and Methods

The main aspects of each procedure are described in this section. Additional details are provided in *SI Appendix*, Note S12.

Liquid Analyte Delivery (Passive approach). The unary compounds or binary mixtures consisted of pentane, anhydrous, ≥99%; hexane, anhydrous, 95%; heptane anhydrous, ≥99%; octane, reagent grade, 98%; nonane, anhydrous, ≥99%; decane, ≥95%; toluene, anhydrous, 99.8%; acetone, ≥99.5%; acetonitrile, anhydrous, 99.8% (Millipore Sigma, used without modification). Aliquots of 1.3 mL of the analyte solvent were injected using a syringe pump (Harvard Apparatus, Holliston, MA) and a 5-mL plastic syringe (Avantor, VWR Incorporation, Randor, PA) at 6 mL min^{-1} into a precleaned Hellma® glass chamber containing a Bragg stack.

Gas Analyte Delivery (Active Sniffing Approach). We constructed a custom chamber (72.6 mm × 25.4 mm × 19.1 mm) consisting of an aluminum case with glass plates at the top and bottom. On each side of the chamber, an inlet and outlet were connected to a set of four 15-mL Falcon tubes and a fume hood, respectively. Each Falcon tube was connected to a solenoid valve (Clippard, Cincinnati, OH) attached to a pressurized nitrogen cylinder at 5 psi. The solenoid valves were controlled via an Arduino board (Teensy 3.2 board with IDE 2.0.2, New York, NY). Three of the four Falcon tubes were filled to the 12-mL mark and one Falcon tube left empty to flow nitrogen. Before each experiment, the sensor chamber was purged by dry nitrogen for 300 s.

Time-Dependent Reflectance Measurements. Reflectance measurements between 400 and 800 nm were obtained with a USB2000+ Fiber Optic Spectrometer (Ocean Optics, Dunedin, FL) and LS-1-CAL tungsten-halogen light source (Ocean Optics) connected via a reflection probe, model R200-7-SR (Ocean Optics), at normal incidence. Measurements were acquired at 1 Hz beginning 15 s before the chemical was injected and for a total of 10 min for the passive delivery case, and at 20 Hz for a total of 12.5 s for the active delivery. Wavelengths between 400 and 800 nm were used for analysis.

Fabrication of Photonic Crystals. The fabrication of the silica and titania Bragg stack was previously described (39). All starting compounds were obtained from Millipore Sigma. Titania nanoparticles were prepared through sol-gel hydrolysis by slowly adding Titanium (IV) ethoxide to 0.1 N HNO_3 and stirring at 80 °C for 8 h. After sonication (Branson Ultrasonics, St. Louis, MI), the particles were filtered and diluted with deionized water. Poly(ethylene oxide) (PEG 8,000-10,000) was added to aid the spin-coating process. SiO_2 colloids (LUDOX SM30, 30 wt.% aq.) were diluted with distilled water to a ratio of 2:5 using hydrophilic syringe filters (SPARTAN 13, 0.2 μm). Bragg stacks were assembled on microscopy slides (VWR Inc.) treated with oxygen plasma (Diener Femto PCCE, Ebhausen, Germany) prior to assembly. The slides were covered with 200 to 250 μL of the silica suspension and spun-coated for 60 s at 2,500 to 5,500 rpm with an acceleration of 1,500 rpm s^{-1} using spin coater (WS-650-23, Laurell, North Wales, PA). Samples were then calcined for 30 min at 350 °C (Lindberg/Blue M BF51866A-1; Thermo Fisher Scientific, Waltham, MA). The procedure was repeated for alternating layers of titania and silica for a total of 5.5 bilayers.

Data Processing. To calculate the feature Ψ(t) for each spectrum, the following steps were performed: a discrete FT was applied to the spectrum, extracting the real and imaginary components of the first nonzero component to calculate the sine of the temporal phase. To reduce noise, a Savitzky–Golay filter with a window size of 31 and polynomial order of three was applied. In the case of passive vapor delivery, the discrete time derivative of Ψ(t), (ΔΨ/Δt), was calculated and then filtered using a Savitzky–Golay filter with a window size of 31 and polynomial order of two. For training ML models, Ψ was normalized using z-score normalization, and ΔΨ/Δt was normalized using the L2-norm. For more details of the data preprocessing and ML hyperparameters refer to *SI Appendix*, Notes S2 and S12, respectively.

Downloaded from https://www.pnas.org by UNIVERSITEIT TWENTE CENTRALE BIBLIOTHEEK on January 9, 2024 from IP address 130.89.47.46.

Algorithms and Computer Codes. The source code and implementation details of temporal analysis and SVMs are available on GitHub https://github.com/soerenbrandt/sniffing-sensor.

Statistical Analysis. Errors in prediction are reported as SD, and all data are represented as mean ± SD, unless otherwise stated.

Data, Materials, and Software Availability. The data is available at (66) and the software is available at https://github.com/soerenbrandt/sniffing-sensor.

ACKNOWLEDGMENTS. We thank Dr. Ian Burgess, Theresa Kay, Dr. Elijah Shirman, Dr. Victoria Hwang, and Dr. Michael Aizenberg for extensive discussions; Tom Blough, Qin Ji, Jake Ferguson, Edrik Lin, and Adam Tetrault for experimental support; and Dr. Edward Soucy for helping design and build the casing for the sniffing sensor chamber. This work was supported by the NSF through the Harvard University Materials Research Science and Engineering Center under award DMR-2011754 and the Kavli Institute for Bionano Science & Technology at Harvard University.

Author affiliations: [a]John A. Paulson School of Engineering and Applied Sciences, Harvard University, Boston, MA 02134; [b]Wyss Institute for Biologically Inspired Engineering, Harvard University, Cambridge, MA 02138; [c]Max Planck Institute for Solid State Research, Stuttgart 70569, Germany; [d]Department of Chemistry, Ludwig-Maximilians-Universität München, München 81377, Germany; [e]Department of Physics, Virginia Polytechnic Institute and State University, Blacksburg, VA 24061; [f]Center for Soft Matter and Biological Physics, Virginia Polytechnic Institute and State University, Blacksburg, VA 24061; [g]Department of Thermal and Fluid Engineering, Faculty of Engineering Technology, University of Twente, Enschede 7522 NB, Netherlands; [h]Department of Molecular and Cellular Biology, Harvard University, Cambridge, MA 02138; [i]Center for Brain Science, Harvard University, Cambridge, MA 02138; and [j]Department of Chemistry and Chemical Biology, Harvard University, Cambridge, MA 02138

1. S. Li, A. Simonian, B. A. Chin, Sensors for agriculture and the food industry. *Electrochem. Soc. Interface* **19**, 41 (2010).
2. B. Szulczyński, J. Gębicki, Currently commercially available chemical sensors employed for detection of volatile organic compounds in outdoor and indoor air. *Environments* **4**, 21 (2017).
3. F. Biasioli, F. Gasperi, C. Yeretzian, T. D. Märk, PTR-MS monitoring of VOCs and BVOCs in food science and technology. *TrAC Trends Anal. Chem.* **30**, 968–977 (2011).
4. R. E. Amor, M. K. Nakhleh, O. Barash, H. Haick, Breath analysis of cancer in the present and the future. *Eur. Respir. Rev.* **28**, 190002 (2019).
5. A. Amann *et al.*, The human volatilome: Volatile organic compounds (VOCs) in exhaled breath, skin emanations, urine, feces and saliva. *J. Breath Res.* **8**, 034001 (2014).
6. T. Wasilewski, J. Gębicki, Emerging strategies for enhancing detection of explosives by artificial olfaction. *Microchem. J.* **164**, 106025 (2021).
7. T. L. Andrew, T. M. Swager, Detection of explosives via photolytic cleavage of nitroesters and nitramines. *J. Org. Chem.* **76**, 2976–2993 (2011).
8. H. Yan, B. Han, H. Siesler, Handheld near-infrared spectrometers: Reality and empty promises. *Spectroscopy* **35**, 15–18 (2020).
9. L. Sela, N. Sobel, Human olfaction: A constant state of change-blindness. *Exp. Brain Res.* **205**, 13–29 (2010).
10. V. N. Murthy, Olfactory maps in the brain. *Annu. Rev. Neurosci.* **34**, 233–258 (2011).
11. M. K. Baller *et al.*, A cantilever array-based artificial nose. *Ultramicroscopy* **82**, 1–9 (2000).
12. D. Zwicker, A. Murugan, M. P. Brenner, Receptor arrays optimized for natural odor statistics. *Proc. Natl. Acad. Sci.* **113**, 5570–5575 (2016).
13. J. M. Schnorr, D. van der Zwaag, J. J. Walish, Y. Weizmann, T. M. Swager, Sensory arrays of covalently functionalized single-walled carbon nanotubes for explosive detection. *Adv. Funct. Mat.* **23**, 5285–5291 (2013).
14. R. A. Potyrailo, N. Karker, M. A. Carpenter, A. Minnick, Multivariable bio-inspired photonic sensors for non-condensable gases. *J. Opt.* **20**, 024006 (2018).
15. R. A. Potyrailo *et al.*, Towards outperforming conventional sensor arrays with fabricated individual photonic vapour sensors inspired by morpho butterflies. *Nat. Commun.* **6**, 1–12 (2015).
16. R. Vishinkin, H. Haick, Nanoscale sensor technologies for disease detection via volatolomics. *Small* **11**, 6142–6164 (2015).
17. Y. Y. Broza, R. Vishinkin, O. Barash, M. K. Nakhleh, H. Haick, Synergy between nanomaterials and volatile organic compounds for non-invasive medical evaluation. *Chem. Soc. Rev.* **47**, 4781–4859 (2018).
18. G. Konvalina, H. Haick, Sensors for breath testing: from nanomaterials to comprehensive disease detection. *Acc. Chem. Res.* **47**, 66–76 (2014).
19. S. Kim *et al.*, Nanoengineering approaches toward artificial nose. *Front. Chem.* **9**, 629329 (2021).
20. R. A. Potyrailo, Multivariable sensors for ubiquitous monitoring of gases in the era of internet of things and industrial internet. *Chem. Rev.* **116**, 11877–11923 (2016).
21. M. Khatib, H. Haick, Sensors for volatile organic compounds. *ACS Nano* **16**, 7080–7115 (2022).
22. A. G. St James *et al.*, Exploring machine learning in chemistry through the classification of spectra: An undergraduate project. *J. Chem. Educ.* **100**, 1343–1350 (2023).
23. C.-Y. Wang, T.-S. Ko, C.-C. Hsu, Interpreting convolutional neural network for real-time volatile organic compounds detection and classification using optical emission spectroscopy of plasma. *Anal. Chim. Acta* **1179**, 338822 (2021).
24. H. Zhou, L. Xu, Z. Ren, J. Zhu, C. Lee, Machine learning-augmented surface-enhanced spectroscopy toward next-generation molecular diagnostics. *Nanoscale Adv.* **5**, 538–570 (2023).
25. M. M. Mozell, Evidence for a chromatographic model of olfaction. *J. General Physiol.* **56**, 46–63 (1970).
26. B. A. Craven, E. G. Paterson, G. S. Settles, The fluid dynamics of canine olfaction: Unique nasal airflow patterns as an explanation of macrosmia. *J. R. Soc. Interface* **7**, 933–943 (2010).
27. T. L. Kelly, A. Garcia Sega, M. J. Sailor, Identification and quantification of organic vapors by time-resolved diffusion in stacked mesoporous photonic crystals. *Nano Lett.* **11**, 3169–3173 (2011).
28. S. E. Létant, M. J. Sailor, Molecular identification by time-resolved interferometry in a porous silicon film. *Adv. Mater.* **13**, 335–338 (2001).
29. Y. Zhang, Q. Fu, J. Ge, Photonic sensing of organic solvents through geometric study of dynamic reflection spectrum. *Nat. Commun.* **6**, 7510 (2015).
30. C. Xiong *et al.*, Detection of homologue and isomer vapors through dynamic reflection spectra of hollow mesoporous silica sphere photonic crystals. *Chem. Asian J.* **13**, 3670–3675 (2018).
31. V. Schroeder *et al.*, Chemiresistive sensor array and machine learning classification of food. *ACS Sens.* **4**, 2101–2108 (2019).
32. I. Sasaki, J. Janata, A. Glezer, Fast gas sensing using an integrated synthetic jet actuator. *IEEE Sens. J.* **6**, 1728–1733 (2006).
33. A. Szczurek, M. Maciejewska, "Artificial Sniffing" Based on induced temporary disturbance of gas sensor response. *Sens. Actuators B Chem.* **186**, 109–116 (2013).
34. S. Nakata, T. Nakamura, K. Kato, Y. Kato, K. Yoshikawa, Discrimination and quantification of flammable gases with a SnO2 sniffing sensor. *Analyst* **125**, 517–522 (2000).
35. T. L. Spencer, A. Clark, J. Fonollosa, E. Virot, D. L. Hu, Sniffing speeds up chemical detection by controlling air-flows near sensors. *Nat. Commun.* **12**, 1232 (2021).
36. P. Shakya, E. Kennedy, C. Rose, J. K. Rosenstein, High-dimensional time series feature extraction for low-cost machine olfaction. *IEEE Sens. J.* **21**, 2495–2504 (2021).
37. S. Y. Choi, M. Mamak, G. Von Freymann, N. Chopra, G. A. Ozin, Mesoporous bragg stack color tunable sensors. *Nano Lett.* **6**, 2456–2461 (2006).
38. S. Colodrero, M. Ocaña, A. R. González-Elipe, H. Míguez, Response of nanoparticle-based one-dimensional photonic crystals to ambient vapor pressure. *Langmuir* **24**, 9135–9139 (2008).
39. I. Pavlichenko *et al.*, Humidity-enhanced thermally tunable TiO 2/SiO 2 bragg stacks. *J. Phys. Chem. C* **116**, 298–305 (2012).
40. T. J. H. Vlugt, R. Krishna, B. Smit, Molecular simulations of adsorption isotherms for linear and branched alkanes and their mixtures in silicalite. *J. Phys. Chem. B* **103**, 1102–1118 (1999).
41. S. Luo, J. L. Lutkenhaus, H. Nasrabadi, Confinement-induced supercriticality and phase equilibria of hydrocarbons in nanopores. *Langmuir* **32**, 11506–11513 (2016).
42. G. Y. Gor *et al.*, Adsorption of n-pentane on mesoporous silica and adsorbent deformation. *Langmuir* **29**, 8601–8608 (2013).
43. J. S. Murguía *et al.*, Two-dimensional wavelet transform feature extraction for porous silicon chemical sensors. *Anal. Chim. Acta* **785**, 1–15 (2013).
44. I. Pavlichenko *et al.*, Bringing one-dimensional photonic crystals to a new light: An electrophotonic platform for chemical mass transport visualisation and cell monitoring. *Mater. Horiz.* **2**, 299–308 (2015).
45. S. Inagaki, Y. Fukushima, Adsorption of water vapor and hydrophobicity of ordered mesoporous silica, FSM-16. *Microporous Mesoporous Mater.* **21**, 667–672 (1998).
46. Y. Matsumura, K. Yamabe, H. Takahashi, The effects of hydrophilic structures of active carbon on the adsorption of benzene and methanol vapors. *Carbon* **23**, 263–271 (1985).
47. F. G. Tenn, R. W. Missen, A study of the condensation of binary vapors of miscible liquids: Part I: The equilibrium relations. *Can. J. Chem. Eng.* **41**, 12–14 (1963).
48. P. Rice, A. El-Nikheli, Isothermal vapour-liquid equilibrium data for the systems n-pentane with n-hexane, n-octane and n-decane. *Fluid Phase Equilibria* **107**, 257–267 (1995).
49. M. Vidal, W. J. Rogers, J. C. Holste, M. S. Mannan, A review of estimation methods for flash points and flammability limits. *Process Saf. Prog.* **23**, 47–55 (2004).
50. M. E. Staymates *et al.*, Biomimetic sniffing improves the detection performance of a 3D printed nose of a dog and a commercial trace vapor detector. *Sci. Rep.* **6**, 1–10 (2016).
51. M. Wachowiak, All in a sniff: Olfaction as a model for active sensing. *Neuron* **71**, 962–973 (2011).
52. P. Qin *et al.*, VOC mixture sensing with a MOF film sensor array: detection and discrimination of xylene isomers and their ternary blends. *ACS Sens.* **7**, 1666–1675 (2022).
53. J. Frittelli, *U.S. Rail Transportation of Crude Oil: Background and Issues for Congress*. Congressional Research Service, pp. 1–29 (2014).
54. V. E. Negus, Humidification of the air passages. *Thorax* **7**, 148–151 (1952).
55. D. Zwicker, R. Ostilla-Mónico, D. E. Lieberman, M. P. Brenner, Physical and geometric constraints shape the labyrinth-like nasal cavity. *Proc. Natl. Acad. Sci. U.S.A.* **115**, 2936–2941 (2018).
56. P. A. Russo, M. M. L. R. Carrott, P. J. M. Carrott, Hydrocarbons adsorption on templated mesoporous materials: Effect of the pore size, geometry and surface chemistry. *New J. Chem.* **35**, 407–416 (2011).
57. Y. Yue, J. P. Gong, Tunable one-dimensional photonic crystals from soft materials. *J. Photochem. Photobiol. C Photochem. Rev.* **23**, 45–67 (2015).
58. R. Kahana-Zweig *et al.*, Measuring and characterizing the human nasal cycle. *PLOS One* **11**, e0162918 (2016).
59. Y. Liu *et al.*, Materials discovery and design using machine learning. *J. Materiomics* **3**, 159–177 (2017).
60. S. Vembu, A. Vergara, M. K. Muezzinoglu, R. Huerta, On time series features and kernels for machine olfaction. *Sens. Actuators B Chem.* **174**, 535–546 (2012).
61. A. D. Rygg, B. Van Valkenburgh, B. A. Craven, The influence of sniffing on airflow and odorant deposition in the canine nasal cavity. *Chem. Senses* **42**, 683–698 (2017).
62. N. Vadamalraj, K. Zingre, S. Seshadhri, P. Arjunan, S. Srinivasan, Hybrid ventilation system and soft-sensors for maintaining indoor air quality and thermal comfort in buildings. *Atmosphere* **11**, 110 (2020).
63. M. Zhou *et al.*, Rapid breath analysis for acute respiratory distress syndrome diagnostics using a portable two-dimensional gas chromatography device. *Anal. Bioanal. Chem.* **411**, 6435–6447 (2019).
64. Q. Liang *et al.*, Ultrasensitive multispecies spectroscopic breath analysis for real-time health monitoring and diagnostics. *Proc. Natl. Acad. Sci. U.S.A.* **118**, e2105063118 (2021).
65. M. M. Y. R. Riad, Y. M. Sabry and D. Khalil, "On the Detection of Volatile Organic Compounds (VOCs) Using Machine Learning and FTIR Spectroscopy for Air Quality Monitoring," 36th National Radio Science Conference, IEEE, pp. 386-392, (2019) doi: 10.1109/NRSC.2019.8734644.
66. S. Brandt, *et al.*, "Data for Non-Equilibrium Sensing of Volatile Compounds Using Active and Passive Analyte Delivery [Data set]." Zenodo. https://doi.org/10.5281/zenodo.7710595 (2023).

Downloaded from https://www.pnas.org by UNIVERSITEIT TWENTE CENTRALE BIBLIOTHEEK on January 9, 2024 from IP address 130.89.47.46.